Direct measurement of DNA bending by type IIA topoisomerases: implications for non-equilibrium topology simplification

Ashley H. Hardin[1,2], Susanta K. Sarkar[1], Yeonee Seol[1], Grace F. Liou[3], Neil Osheroff[4,5] and Keir C. Neuman[1,*]

[1]Laboratory of Molecular Biophysics, National Heart, Lung, and Blood Institute, National Institutes of Health, Bethesda, MD 20892, [2]Institute for Physical Science and Technology, University of Maryland, College Park, MD 20742, [3]Laboratory of Chemical Physics, National Institute of Diabetes and Digestive and Kidney Diseases, National Institutes of Health, Bethesda, MD 20892 and [4]Department of Biochemistry and [5]Department of Medicine, Vanderbilt University School of Medicine, Nashville, TN 37232, USA

ABSTRACT

Type IIA topoisomerases modify DNA topology by passing one segment of duplex DNA (transfer or T–segment) through a transient double-strand break in a second segment of DNA (gate or G–segment) in an ATP-dependent reaction. Type IIA topoisomerases decatenate, unknot and relax supercoiled DNA to levels below equilibrium, resulting in global topology simplification. The mechanism underlying this non-equilibrium topology simplification remains speculative. The bend angle model postulates that non-equilibrium topology simplification scales with the bend angle imposed on the G–segment DNA by the binding of a type IIA topoisomerase. To test this bend angle model, we used atomic force microscopy and single-molecule Förster resonance energy transfer to measure the extent of bending imposed on DNA by three type IIA topoisomerases that span the range of topology simplification activity. We found that *Escherichia coli* topoisomerase IV, yeast topoisomerase II and human topoisomerase IIα each bend DNA to a similar degree. These data suggest that DNA bending is not the sole determinant of non-equilibrium topology simplification. Rather, they suggest a fundamental and conserved role for DNA bending in the enzymatic cycle of type IIA topoisomerases.

INTRODUCTION

Topoisomerases are enzymes that modify and regulate the topology of cellular DNA (1–5). The regulation of DNA topology is essential in all organisms since vital cell processes, such as DNA replication and transcription, give rise to a myriad of topological problems, including knotting, catenation and excess supercoiling of genomic DNA.

Type I topoisomerases cut a single strand of DNA through an ATP-independent mechanism that allows for the relaxation of supercoils and, in some cases, passage of duplex DNA through a nick (2). Type II topoisomerases, on the other hand, cut both strands of one segment of DNA (gate or G–segment) and pass a second segment (transfer or T–segment) through the transient double-strand break via an ATP-dependent mechanism (Figure 1A) (1–3,5). This two-gate mechanism results in unidirectional strand passage (6,7). Though they share a similar core strand passage mechanism, the type II topoisomerase subclasses, type IIA and type IIB, are structurally, biochemically and evolutionarily distinct (8–10). Type IIA topoisomerases are capable of relaxing and introducing supercoils, as well as generating and removing intramolecular and intermolecular links, i.e. knots and catenanes. Type IIA topoisomerases play a fundamental role in chromosome segregation during cell division by unlinking catenated sister chromatids thus enabling daughter cells to receive the proper complement of chromosomes (3). They are also likely required to reduce the level of DNA knotting that is expected in highly compacted DNA, which would have deleterious consequences
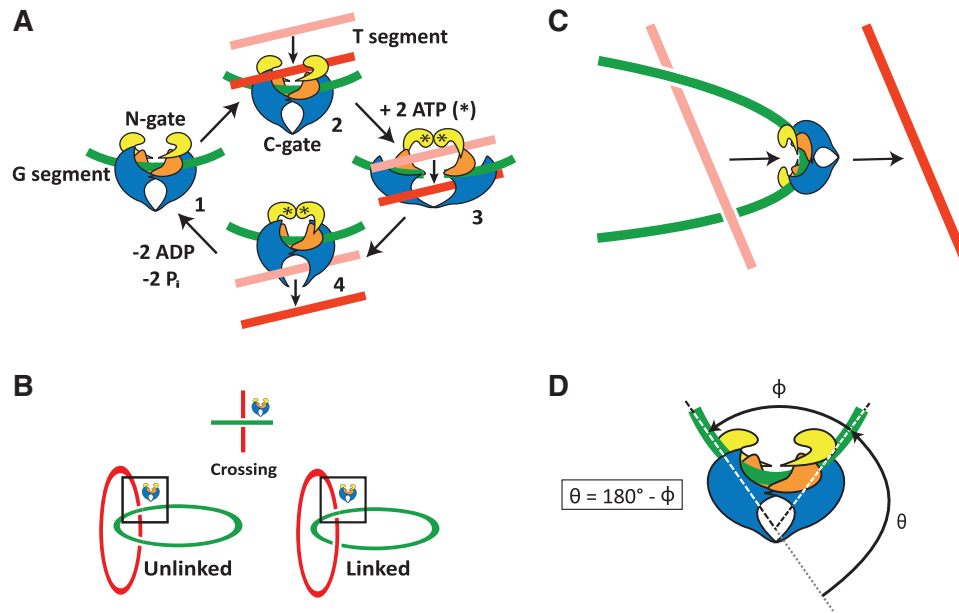
Figure 1. The interaction of type IIA topoisomerases with DNA. (**A**) Core strand-passage mechanism for type IIA topoisomerases [adapted from Bates and Maxwell (7)]. (1) Type IIA topoisomerase (blue, yellow and orange) binds duplex G–segment DNA (green). (2) A second duplex, T–segment DNA, (pink to red, denoting movement of the DNA) subsequently binds to the topoisomerase. (3) Upon binding two ATP molecules (asterisks), the N–gate (yellow) closes, trapping the T–segment inside the ATP-binding 'clamp' and the G–segment is cleaved, permitting passage of the T–segment. (4) The G–segment is religated, and the T–segment is released from the C–gate (blue) of the topoisomerase. ATP hydrolysis products, ADP and P_i, are then released, resetting the enzyme for another strand passage event. (**B**) A topoisomerase located at a single DNA crossing cannot directly differentiate between an unlinked and a linked conformation. (**C**) The bend angle model posits that a type IIA topoisomerase induces a sharp bend in the G–segment DNA, orienting the active site of the enzyme toward the interior of the bend. This geometry favors the capture of a T–segment from inside rather than outside the bend. (**D**) The bend angle, θ, is defined as the angle through which the DNA is bent from a straight line. The opening angle, ϕ, measured between the two DNA segments emerging from the topoisomerase, is the supplement of the bend angle, hence $\theta = 180 - \phi$.

if allowed to accumulate (11–14). Though type IIA topoisomerases facilitate these critical unlinking and unknotting processes via a strand-passage mechanism, random strand-passage would not lead to specific and complete unlinking and unknotting (15). Rather, it would result in a dynamic equilibrium between linking and unlinking reactions.

Rybenkov *et al.* (15) showed that non-supercoiling type IIA topoisomerases (i.e. type IIA topoisomerases with the exception of DNA gyrase, which negatively supercoils DNA) simplify the global topology of DNA, shifting it away from an equilibrium distribution of catenanes, knots and supercoils toward a less entangled topology. An equilibrium distribution, referred to as topological equilibrium, of knots, catenanes and supercoils is achieved if every encounter between two DNA segments has an equal probability of resulting in strand passage. Because type I topoisomerases do not consume energy, they shift DNA topology toward equilibrium. In contrast, type IIA topoisomerases can shift global topology away from equilibrium, which implies that they couple topology sensing to strand passage to achieve preferential simplification of knots, catenanes and supercoils. Since type IIA topoisomerases consume ATP, thermodynamic principles are not violated, but the mechanism by which the energy of ATP hydrolysis is coupled to topology simplification remains elusive (16). Specifically, it is unclear how an enzyme that acts on the scale of nanometers is able to assess the global topology of DNA. If the enzyme only interacts with a single DNA crossing, how is

it able to determine that a strand passage event would result in the removal, rather than the creation, of a linkage (Figure 1B)?

Several mechanistic models of topology simplification by type IIA topoisomerases have been proposed (15, 17–21), though to date the experimental evidence distinguishing them has been equivocal (22). One of the leading and theoretically well-characterized models is the G–segment bend angle model. This model, originally proposed by Vologodskii *et al.* (19) and later expanded upon by Klenin *et al.* (20), postulates that non-supercoiling type IIA topoisomerases introduce a sharp bend in the G–segment DNA that localizes the active site of the enzyme to the interior apex of the bent DNA (Figure 1C). The bend orients the topoisomerase such that the T–segment binding site of the enzyme tends to point toward the inside of circular DNA, favoring strand passage from the interior to the exterior of the circle. This geometric selection, coupled with the unidirectional strand passage embodied in the two gate mechanism of type IIA topoisomerases, would lead to preferential unlinking, unknotting and supercoil relaxation. The bend angle model further postulates that topology simplification activity scales with the magnitude of the imposed bend angle, providing a mechanistic basis for the observed variation in non-equilibrium simplification activities among different type IIA topoisomerases (15,16).

Recent studies, including structures of gram positive *Streptococcus pneumoniae* topoisomerase IV (23) and

gram negative *Acinetobacter baumannii* topoisomerase IV (24), both co-crystallized with DNA in a covalently bound cleavage complex, structures of yeast topoisomerase II (yTopo II) co-crystallized both with non-covalently bound DNA (25) and in a covalently bound DNA cleavage complex (26), and single-molecule magnetic tweezers measurements (27), indicate that DNA is bent by type IIA topoisomerases. Though these studies lend support to the bend angle model, other studies give contradictory results. For instance, recent simulations using an improved worm-like chain (WLC) model have shown that a sharply bent conformation of the G–segment DNA is not sufficient to reproduce experimental non-equilibrium topology simplification results (28,29). Also, an implication of the bend angle model is that topology simplification activity should depend on DNA circle size. Decreasing the circle size should increase the probability that a bend would orient the active site of the enzyme toward the interior of the circle. This, in turn, would be expected to amplify the effect of the bend angle, thereby enhancing topology simplification activity. However, the non-equilibrium activity of yTopo II and *Escherichia coli* topoisomerase IV (Topo IV) appear to be independent of DNA circle size for circles large enough to adopt more than two topoisomer conformations (16,21). Although these various results either indirectly support or contradict the bend angle model, the specific predictions of the model have not been tested directly (22).

In this study, we used atomic force microscopy (AFM) to image type IIA topoisomerase-DNA complexes and directly measure the bend angles imposed on the DNA by three non-supercoiling type IIA topoisomerases that span the range of topology simplification activity: Topo IV, human topoisomerase IIα (hTopo IIα) and yTopo II, in order of decreasing non-equilibrium topology simplification activity (15,16). We also used ensemble and single-molecule Förster resonance energy transfer (FRET) to probe the extent of DNA bending by these three topoisomerases. According to the bend angle model, Topo IV, which has the largest simplification activity, should impose the largest bend in DNA, whereas yTopo II, which has the smallest simplification activity, should impose the smallest bend (20). The bend angles imposed on the DNA by each of these proteins measured by AFM and computed from FRET efficiencies were compared to those predicted by the bend angle model. We found that all three type IIA topoisomerases bent the DNA to a similar degree. Moreover, for each enzyme, with the possible exception of yTopo II, the extent of the bending was less than predicted by the bend angle model, which suggests that G–segment DNA bending is unable to fully account for the topology simplification behavior of these enzymes.

MATERIALS AND METHODS

Enzymes and DNA substrates

yTopo II and hTopo IIα were purified as previously described (30,31). ParC and ParE subunits of Topo IV
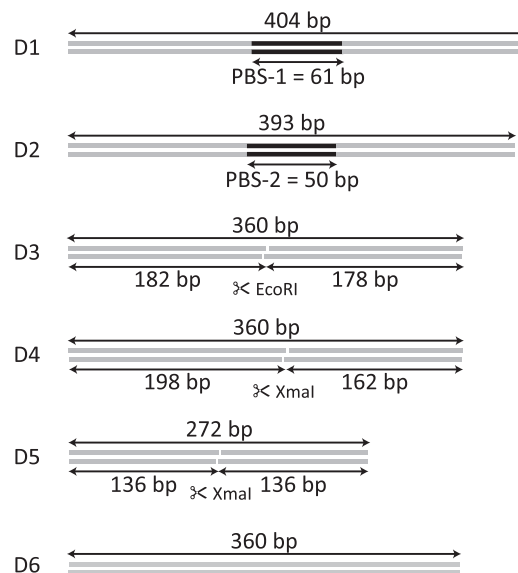

Figure 2. DNA substrates used for AFM imaging. D1 and D2 contain putative Topo IV binding sequences PBS–1 and PBS–2, respectively (see main text for sequence). D3–D5 were digested with the restriction enzyme indicated. D6 is identical in sequence to D3 and D4 but undigested. All DNA substrates were made by PCR, based on the multiple cloning site of pUC19 plasmid.

were purified as previously described (32) with minor modifications. Briefly, the cell pellet was resuspended in 20 mM HEPES (pH 7.5), 400 mM NaCl, 10% glycerol and 2 mM β-mercaptoethanol, lysed by sonication and centrifuged. The supernatant was loaded onto a HisTrap HP column (GE Healthcare, Piscataway, NJ, USA) and the protein was eluted with a linear gradient of 0–200 mM imidazole. The protein containing fractions were pooled and desalted on a HiPrep desalting column (GE Healthcare). The His-tag was removed by overnight incubation with AcTEV (33) at 4°C using an OD_{280nm} ratio of 1:100 AcTEV:protein and the cleaved protein was filtered through a HisTrap HP column. The protein was concentrated and further purified on a Superdex 200 10/300 GL column (GE Healthcare). ParC and ParE were quantified by UV absorption, and the complexes were assembled by incubating equimolar quantities of ParC and ParE subunits on ice.

The AFM—DNA substrates are illustrated in Figure 2. Substrates D1 and D2 are 404 and 393 base pairs (bp) long, respectively, and each contains one of two putative Topo IV binding sequences as determined by Marians and Hiasa (34). Putative binding sequence one (PBS–1) is 5′–GGGCCACTCCTAAAAATCCGGGGTATACCCCGGATTTTTAGGAGTGGCCCGAACCGTTCG–3′, and putative binding sequence two (PBS–2) is 5′–CGCACGGGCCCTAAATAGGGGGGGTATACCCCCCTATTTAGAACCGGTTCG–3′. Substrate D1 was developed by inserting PBS–1 into pUC19 plasmid (New England Biolabs, Ipswitch, MA, USA) between the EcoRI and BamHI restriction sites. The resulting plasmid was amplified by PCR using Phusion DNA polymerase (New England Biolabs), with oligonucleotide primers FOR–1 (5′–GGAGAAAATACCGCATCAGGCGCC–3′) and REV–1 (5′–TGTGAGTTAGCTCACTCATTAGGCAC
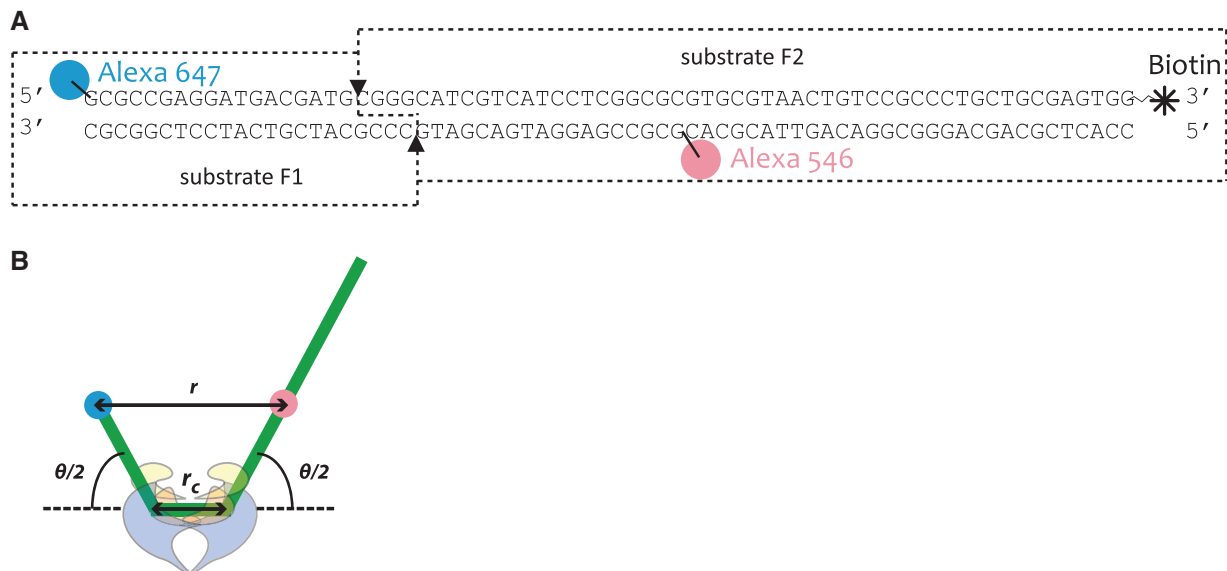
Figure 3. Schematics of single-molecule FRET experiments. (**A**) DNA used in single-molecule FRET experiments showing locations of the fluorophores, Alexa546 and Alexa647, biotin and double-stranded overhang. (**B**) Schematic representation of a type IIA topoisomerase bending the FRET substrate. The distance between the fluorophores (r) was determined from the FRET efficiency measurements [Equation (3)] and related to the bend angle using the relationship shown in Equation (4). Here, r_c is the length of the unbent DNA segment between the two bent DNA segments and r_{tot} (not labeled) is the contour length of DNA between the two fluorophores.

CC–3′). Substrate D2 was constructed in the same manner as D1, but contained PBS–2. Substrates D3 and D4 were designed to improved binding affinity. They are 360 bp long but include a 4 bp staggered double-stranded break at or near the middle of the molecule. Position 217–576 of plasmid pUC19 was amplified by PCR, using primers FOR–1 and REV–1 as described above, and digested with either EcoRI to make D3, XmaI to make D4, or left intact as a control, D6. EcoRI and XmaI were used to vary the sequence of the 4 bp overhang. D5 consists of position 279–550 of pUC19, amplified by PCR using oligonucleotide primers FOR–2 (5′–TCGGTGCGGGCC TCTTCGC–3′) and REV–2 (5′–CCCAGGCTTTACACT TTATGCTTCCGGCTCG–3′). This substrate is 272 bp long and was digested by XmaI at its restriction site, producing equal 136 bp fragments. This is a symmetric version of D4 since it contains much of the same sequence and is cut with the same restriction enzyme. All restriction endonucleases were obtained from New England Biolabs.

DNA substrates used in single-molecule FRET experiments, F1 and F2, were adapted from Dong *et al.* (25) but were lengthened to prevent interaction between the protein and the surface of the glass slide. As shown in Figure 3A, fluorescent DNA substrates F1 and F2 contain a complementary 4 bp overhang that allowed the transiently annealed region to be stabilized by a bound topoisomerase and thus generate a FRET signal. Substrate F1 contains an Alexa647 fluorophore at the 5′ blunt end of the segment. The sequence of the top strand of F1 is: 5′–[Alexa647]-GCGCCGAGGATGACGATG–3′. The sequence of the complementary bottom strand of this substrate is: 3′–CGCGGCTCCTACTGCTAC|GCCC–5′, where the '|' denotes the beginning of the 4 bp overhang

(Figure 3A). Substrate F2 contains an internal Alexa546 fluorphore, located the same distance from the 4 bp overhang as the Alexa647 on F1 and a biotin at the 3′ blunt end. The sequence of the top strand of F2 is: 5′–CGGG|CATCGTCATCCTCGGCGCCGTGCGTAAC TGTCCGCCCTGCTGCGAGTGG-[Biotin]–3′, where the '|' denotes the beginning of the 4 bp overhang. The sequence of the complementary bottom strand is 3′–GT AGCAGTAGGAGCCGCG-[Alexa546]-GCACGCATT GACAGGCGGGACGACGCTCACC–5′ (Figure 3A). Each of these oligos, including the fluorophores and biotin, was synthesized by Eurofins MWG Operon (Huntsville, AL, USA).

Relaxation assays

Wheat germ topoisomerase I (Topo IB) (Promega, Madison, WI, USA), Topo IV, yTopo II and hTopo IIα were incubated with plasmid pBR322 (New England Biolabs) at protein: DNA concentrations of 25 nM: 50 nM in a 60 μl reaction containing 40 mM Tris–HCl (pH 7.5), 6 mM MgCl₂, 100 mM KOAc, 1 mM DTT, 1 mM ATP, 0.1 mM EDTA and 50 μg/ml bovine serum albumin (BSA) (New England Biolabs). Unless otherwise noted, all chemicals were obtained from Sigma-Aldrich (St Louis, MO, USA). Reactions were incubated overnight at 37°C and stopped with a buffer containing 0.1% SDS, 10 mM EDTA and TrackIt™ Cyan/Yellow Loading Buffer (Invitrogen, Carlsbad, CA, USA). A 1% Tris–Acetate EDTA (TAE) agarose gel containing 1 μg/ml chloroquine was loaded with 10 μl of reaction. Gels were run overnight at 2.5 V/cm at 4°C in 1× TAE supplemented with 1 μg/ml chloroquine to resolve topoisomers, destained in water for 2 h to remove chloroquine, and stained for 40 min in a solution of 1× SYBR® Green I

nucleic acid stain prior to imaging with a Biospectrum® AC Imaging System (UVP, Upland, CA, USA). VisionworksLS (UVP) and ImageJ (National Institutes of Health, Bethesda, MD, USA) software were used to obtain and analyze gel intensity profiles.

Protein–DNA complex formation

Topo IV (300 nM-2.4 μM) and DNA (60 nM-480 nM) were incubated on ice for 30 min, at a protein:DNA ratio of 5:1 for all reactions. Binding buffers 1–4: BB1 [50 mM HEPES (pH 7.5), 5 mM $MgCl_2$, 50 mM NaCl, and 5% v/v glycerol], BB2 [50 mM Tris–HCl (pH 7.5), 10 mM $MgCl_2$, 20 mM KCl, 5 mM DTT and 2.5% v/v glycerol], BB3 [50 mM Tris–HCl (pH 7.5), 10 mM $MgCl_2$, 10 mM KCl, 5 mM DTT and 2.5% v/v glycerol], and BB4 [50 mM Tris–HCl (pH 7.5), 10 mM CaOAc, 12.5 mM sodium malonate, 5 mM DTT and 5% v/v glycerol] were used for the incubation reactions of Topo IV with DNA substrates D1–D5. Some of the Topo IV–DNA reactions in BB1 and BB2 were supplemented with 50 μM quinolone (norfloxacin, ciprofloxacin or levofloxacin). yTopo II and hTopo IIα were incubated with DNA substrates D4 and D5 under the same conditions as Topo IV, but they were incubated exclusively in BB4. In the binding reactions, the salt concentration of the enzyme storage buffers increased the concentration of NaCl by ∼1 mM for Topo IV, whereas the yTopo II and hTopo IIα storage buffers increased the NaCl concentration by ∼50 mM.

Atomic force microscopy

Complexes were assembled as described above and diluted 8- to 12-fold in deposition buffer [50 mM HEPES (pH 7.5), 5 mM $MgCl_2$, 50 mM NaCl and 2–5% v/v glycerol] to a final protein:DNA concentration of 60 nM:12 nM in a total volume of 20 μl (35). The entire 20 μl sample was immediately deposited on a freshly cleaved mica surface (Spruce Pine Mica Company, Spruce Pine, NC, USA) and allowed to adsorb for ∼30 s at room temperature before being gently rinsed with Milli-Q water for 30 s. Residual water was wicked from the mica using a strip of filter paper, and the mica was gently blown dry with compressed air (Whoosh-Duster™, Control Company, Houston, TX, USA). Images were captured using Multimode JV and EV scanners and Nanoscope IIIa and V controllers (Veeco Metrology, Santa Barbara, CA, USA). Data were collected using tapping mode in air. SSS–NCHR (tip radius <5 nm) (Nanosensors, Neuchatel, Switzerland) and AC160TS (tip radius <10 nm) (Olympus, Tokyo, Japan) tapping mode silicon probes were used for imaging. Both cantilever probes had spring constants of ∼42 N/m and resonance frequencies of ∼300 kHz. Images were collected at a rate of 2–3 Hz and had a resolution of 512 × 512 pixels per square micron.

Image analysis

AFM images were flattened to correct for the natural curvature of the mica surface using Nanoscope V software and converted to bitmap files using WSxM

software (36). DNA bend angles were measured using three different techniques: manual tangent overlay, automated tangent overlay and end-to-end distance (EED) fitting. Manual tangent overlay, was performed as previously described (35,37–39). Briefly, we used the angle measurement tool in ImageJ to measure the angle (ϕ) between two tangent line segments that were drawn along the contour of the ∼50 nm DNA fragments emerging from the ∼15 nm diameter protein (Figures 1D and 5E). The bend angle (θ) is defined as $\theta = 180 - \phi$ (Figure 1D). Three types of protein–DNA complexes were identified: enzyme bound to a long substrate (D1 or D2), enzyme bound to a short substrate (D3, D4, or D5), and enzyme bound and joining two short substrates (D3, D4, or D5) (Figure 2). Protein–DNA complexes were manually selected based on the criteria that only one protein was bound to the DNA, protein was not bound to the ends of the DNA, and the bound DNA did not intersect another DNA molecule. The intrinsic bend angles of free DNA (substrate D6) were determined as described (35,38). Briefly, 15 nm circles were drawn near the middle of each DNA molecule to simulate bound protein and angles were measured as described above for actual protein–DNA complexes. The measured angles (ϕ) determined for unbound DNA were all measured to be <180°. Plotting and statistical analysis was performed with IGOR Pro software (Wavemetrics, Oswego, OR, USA). Data were statistically analyzed using the analysis of variance (ANOVA) and Tukey Tests in IGOR Pro. Each subset of data for Topo IV, corresponding to different substrate and/or buffer conditions, was compared against all other subsets to ensure that the populations were statistically indistinguishable in regards to both the variance (ANOVA) and mean (Tukey Test).

The automated tangent overlay bend angle measurement technique was an automated, image processing based implementation of the manual tangent overlay procedure. This program, written in LabVIEW™ (National Instruments, Austin, TX, USA), first applied a pixel threshold and adjusted the brightness, contrast, and γ-values of each image such that free DNA, unbound topoisomerase, and DNA–topoisomerase complex images were above the background threshold value. Second, the program applied a size threshold such that only the DNA–topoisomerase complex images were above the threshold value, thus filtering out all free DNA and free topoisomerases from the images. Rectangular regions containing images of the DNA–topoisomerase complexes were extracted and stored as sub-image files. Each sub-image window was individually judged by a human supervisor, who would accept or reject complexes based on the same criteria used for manual tangent overlay.

Each selected sub-image was analyzed to determine the bend angle formed by the two DNA segments emerging from the topoisomerase. For each DNA–topoisomerase complex, a circular overlay was fitted to best match the shape of the enzyme, thus estimating its center and radius. Additionally, two concentric circles, centered on the protein, were superimposed on the complex such that the inner circle radius was 2–4 nm larger than the radius

of the topoisomerase and the outer circle radius was 30–60 nm larger than the inner circle. Next, the skeleton of the DNA was extracted after applying a binary threshold to the image and removing small objects surrounding the DNA segments. Sections of the DNA skeletons lying between the two superimposed circles were linearly fitted, and the fits were extrapolated to the point of intersection to determine the angle of intersection, ϕ, which was previously defined as the supplement to the bend angle, θ (Supplementary Figure S1A and Figure 1D). We used the methods of maximum likelihood and bootstrapping to determine the mean, standard deviation and error of the angle distributions.

The EED measurement technique assayed a more global property of bending by comparing measured EEDs with simulated EEDs of bent DNA molecules equilibrated in 2D. We followed the method of Dame *et al.* (40) with two modifications. Briefly, for each DNA substrate, histograms of the EEDs of simulated DNA molecules were generated using WLC statistics with a persistence length of 50 nm for a range of imposed bend angles. These histograms were then compared with the histogram of measured EEDs from the AFM images of topoisomerase–DNA complexes containing two DNA molecules joined by a topoisomerase. The χ^2 statistic was calculated using an expression developed specifically for Poisson distributed data, shown in Equation (1), where $f(x_i, \vec{a})$ are the data from the simulated histogram and n_i are data from the histogram of the experimental data (41). The bend angle was defined as the imposed bend angle of simulated DNA that minimized the χ_P^2 value.

$$\chi_P^2 = \sum_{i=1}^{N} \left[2(f(x_i, \vec{a}) - n_i) + (2n_i + 1) \log\left(\frac{2n_i + 1}{2f(x_i, \vec{a}) + 1} \right) \right] \quad (1)$$

This method was modified to account for the specific details of the DNA substrate used in this study and the binding geometry of type IIA topoisomerases (23,25,26). As shown in Figure 2, DNA substrates of varying lengths were used for the AFM imaging. In particular, substrates in which the restriction fragments were of unequal lengths could form three possible complexes with a topoisomerase stabilizing the palindromic 4 bp junction: the long fragment could bind to the shorter fragment with a probability of 0.5, the long fragment could bind to another long fragment with a probability of 0.25, or the short fragment could bind to another short fragment with a probability of 0.25. We accounted for this ambiguity in the bound substrates by simulating all possibilities and combining the simulations with the appropriate statistical weight (0.5 or 0.25). In other words, each simulated distribution was made up of 50% long–short, 25% long–long and 25% long–short DNA complexes.

The second alteration of this method involved simulating a two-kink model of DNA bending instead of the one-kink bending model utilized by Dame *et al.* (40). In a one-kink model, the DNA is kinked in one position, creating a 'V' shape. In a two-kink model, the DNA is kinked in two positions, creating a flat-bottomed 'V', where the length of the flat bottom is held constant, and

for the purpose of these simulations was assumed to be rigid (R_c) (Supplementary Figure S1B). Instead of imposing one bend of θ degrees, we imposed two bends, each $\theta/2$ degrees, on either side of the R_c segment of the DNA. We held the length constant in the R_c region for each simulation, but ran the simulation for four different values of R_c: 0, 2, 4 and 6 nm. Then, as in the original method, we used WLC statistics to model the segments of the DNA from the location of the bends to the ends of the DNA molecules. Because crystal structure data indicate that type IIA topoisomerases bend DNA by imposing two bends on either side of a straight segment of DNA (23,25,26,42), we reasoned that the two-kink model of DNA bending would be more appropriate for our data than the one-kink model.

In addition to the bend angles determined by comparing the histograms of simulated data to experimental data, we also used a χ^2 statistic [Equation (2)] to compare the mean square EEDs for the simulated and experimental data (43). Here, $\langle R_{\text{sim}}^2 \rangle$ is the mean square EED of the simulated DNA for a given bend angle, $\langle R^2 \rangle$ is the measured mean square EED, and σ^2 is the variance of the mean square EED measurement. Supplementary Figure S2 shows a representative histogram of experimental EED data and the best fit histogram of simulated DNA, as well as the plots of χ_P^2 as a function of bend angle for the simulated histogram data and $\chi_{\langle R^2 \rangle}^2$ as a function of bend angle for the mean square EEDs.

$$\chi_{\langle R^2 \rangle}^2 = \frac{\left(\langle R_{\text{sim}}^2 \rangle - \langle R^2 \rangle \right)^2}{\sigma^2} \quad (2)$$

Single molecule FRET experiments

A custom-built prism-type total internal reflection (TIR) fluorescence microscope based on an Olympus IX71 was used to measure bend angles at the single-molecule level. A flow cell was constructed with double-sided tape [SA–S–1L 0.12 mm Grace BioLabs (Bend, OR, USA) Secure-Seal adhesive double-sided tape] sandwiched between a coverslip [Gold Seal (Thermo Scientific, Portsmouth, NH, USA) 1 22 mm × 40 mm] and a quartz slide [SPI (West Chester, PA, USA) 25 mm × 76 mm × 1 mm]. Both the coverslip and the quartz slide were cleaned extensively using NaOH, ethanol and acetone. TIR of the excitation laser was achieved using a quartz prism [CVI (Albuquerque, NM, USA) PLBC–5.0–79.5–SS] and occurred at the interface of the quartz slide and the buffer in the flow cell. The evanescent wave at the interface generated due to TIR was used to excite fluorescently labeled substrates within a thin layer of ~250 nm. The excitation laser, with a power of ~3 mW at 532 nm [CrystaLaser (Reno, NV, USA) GCL–025–L–0.5%], was focused onto an area of ~150 × 150 μm^2 to excite Alexa546 labeled donor substrates. Alexa647 labeled acceptor substrates were used to detect FRET between two substrates due to imposed bending by different type II topoisomerases. Fluorescence was collected by a water immersion objective with 60 × magnification and 1.2 numerical aperture [Olympus (Center Valley, PA, USA) UPLSAPO60XWIR]. Additional magnification of 1.6 × in

the Olympus IX71 was used to obtain a total magnification of 96 ×. Excitation light was rejected using a HQ550LP filter (Chroma, Bellows Falls, VT, USA). Donor emission and acceptor emission were separated using a Dual View [Photometrics (Tucson, AZ, USA) DV2-SYS with 06-EML2 Optical Filter Set] and detected using an EMCCD camera [Andor (South Windsor, CT, USA) DV897DCS–BV]. Andor iQ 1.8 software was used to control the camera and record movies with 100 ms time resolution. Fluorescence intensities of both donor and acceptor as a function of time for individual molecules were extracted for further analysis.

The buffer used in single-molecule FRET experiments was the same used for ensemble activity assays minus ATP: 40 mM Tris–HCl (pH 7.5), 6 mM MgCl$_2$, 1 mM DTT, 100 mM KOAc, 50 μg/ml BSA and 0.1 mM EDTA. For these experiments, a mixture of 25 nM Alexa546 (donor) labeled DNA substrate F1 (Figure 3A), 25 nM Alexa647 (acceptor) labeled DNA substrate F2 (Figure 3A) and 1 μM Type IIA topoisomerase was incubated on ice for 30 min. Three microliters of this mixture was diluted in 1 ml buffer, flowed into the flow cell, and incubated for 10 min to immobilize the donor substrates prior to recording movies. Biotinylated donor substrates (F2, Figure 3A) were immobilized on the quartz surface of the flow cell using a streptavidin-biotin linker. Since the acceptor was on a separate DNA substrate (F1) we observed FRET only when a topoisomerase bound both the donor and acceptor substrates and introduced a bend (Figure 3B). A control experiment with both donor and acceptor substrates but no topoisomerase showed no FRET.

RESULTS

Different type IIA topoisomerases simplify topology to differing degrees

Type IIA topoisomerases have been shown to reduce the topological complexity of DNA by preferentially removing knots and catenanes and reducing the absolute level of supercoiling (15,16). These measures of topology simplification are highly correlated for each type IIA topoisomerase, suggesting that they are likely governed by a single underlying process (15). Thus, supercoil relaxation measurements are sufficient to confirm the non-equilibrium activities of these enzymes (16). In order to verify the non-equilibrium activities of the type IIA topoisomerases used for AFM imaging, we measured supercoil relaxation by Topo IV, yTopo II and hTopo IIα. The absolute level of supercoiling is reflected in the width of the topoisomer distribution, i.e. the relative abundance of each topoisomer. The topoisomer distribution can be resolved on an agarose gel in the presence of chloroquine as shown in Figure 4A. Individual topoisomers differing by a single linking number (Lk) ran as distinct bands in the gel, the relative intensities of which were plotted to obtain the topoisomer distribution. The width of the topoisomer distribution is quantified by the variance (ΔLk^2), with reduced absolute levels of supercoiling
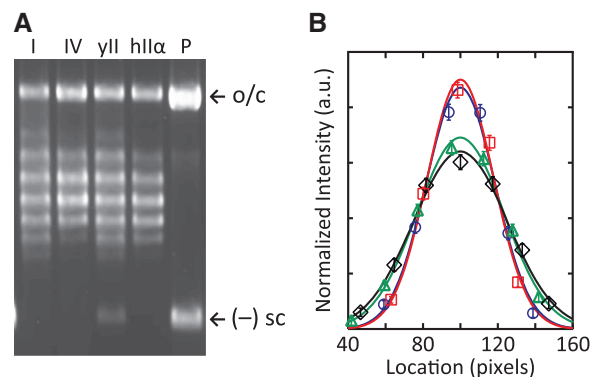

Figure 4. Topology simplification by type IIA topoisomerases. (**A**) Agarose gel run in the presence of 1 μg/ml chloroquine to resolve topoisomers. The bands on the gel correspond to the linking numbers (Lk) of the plasmid DNA. The center band in each lane contains relaxed DNA and bands on either side contain DNA with ΔLk of ±1 for each subsequent band from the center. The topoisomer distributions for wheat germ Topo I (I), Topo IV (IV), yTopo II (yII) and hTopo IIα (hIIα) are shown along with negatively supercoiled plasmid DNA (P). The band at the top of each lane is open circular (nicked) DNA (o/c). (**B**) Normalized topoisomer distributions for each topoisomerase. Points on the graph represent the peak intensity of each band plotted as a function of the peak location in pixels. Each topoisomerase distribution was fit to a Gaussian (lines): Topo I (diamonds, black line), Topo IV (squares, red line), yTopo II (triangles, green line) and hTopo IIα (circles, blue line).

corresponding to reduced variances. As previously observed, the distribution of topoisomers was narrower for the type IIA topoisomerases than for Topo I, which generates an equilibrium distribution of topoisomers. The degree of topological simplification was quantified by comparing the variances of the type IIA topoisomerase distributions with that of the Topo IB distribution. The ratio (R) of the variance of Topo IB to each of the type IIA topoisomerases was consistent with reported values (Figure 4B) (15,16). Topo IV shifted the topology furthest from equilibrium ($R = 1.9 \pm 0.1$; mean ± SD), hTopo IIα shifted the topology to an intermediate extent ($R = 1.8 \pm 0.1$), and yTopo II shifted the topology the least ($R = 1.12 \pm 0.07$).

Type IIA topoisomerases impose comparable bend angles on DNA

The bend angle model posits that the degree of non-equilibrium topology simplification by type IIA topoisomerases depends on the extent of G–segment DNA bending. In order for DNA bending to account for differences in topology simplification, the type IIA topoisomerases we investigated would impose significantly different bend angles, ranging from ~100° for yTopo II to >300° for Topo IV (20). To evaluate the feasibility of this model, we used AFM and single-molecule FRET to determine the differences in G–segment DNA bending among type IIA topoisomerases that exhibit a wide range of non-equilibrium relaxation activities (Figure 4). Figure 5 shows typical AFM images of topoisomerase IIA-DNA complexes as well as DNA in the absence of protein.
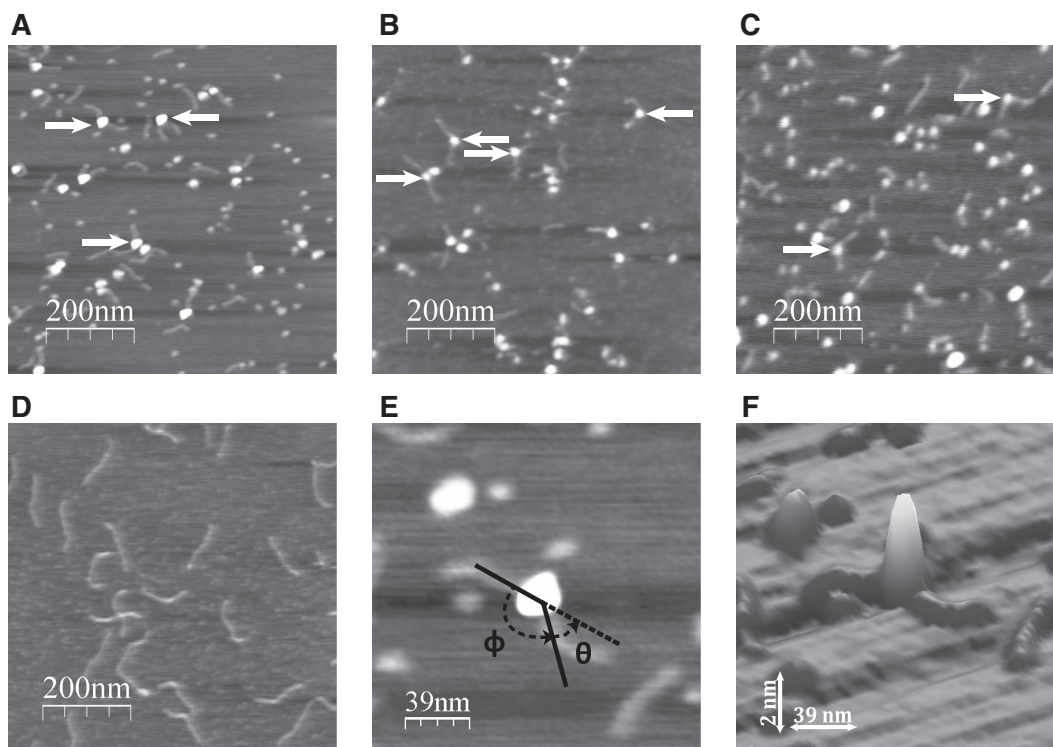
Figure 5. AFM images of DNA–type IIA topoisomerase complexes. (**A**) Representative Topo IV–DNA complexes (designated by white arrows). (**B**) yTopo II–DNA complexes. (**C**) hTopo IIα–DNA complexes. (**D**) DNA in the absence of protein. (**E**) One DNA–Topo IV complex with the measured angle (ϕ) and bend angle (θ) indicated. (**F**) Three-dimensional representation of the complex from (**E**). The vertical scale has been expanded for clarity.

We incubated Topo IV with one of two linear DNA substrates, D1 or D2 (Figure 2), each of which included a putative Topo IV binding sequence adapted from Marians and Hiasa (34). The complexes were deposited on freshly cleaved mica and imaged in air using tapping mode AFM. These substrates exhibited low binding affinity under the conditions required for AFM imaging of protein–DNA complexes (10–60 nM enzyme). Since type IIA topoisomerases have been shown to preferentially bind and stabilize 4 bp complementary overhangs (25), we developed substrates D3 and D4 (Figure 2) that contained complementary 4 bp overhangs to stabilize binding. This binding configuration further provided a high degree of specificity as complexes consisting of two DNA segments joined by a topoisomerase could be easily distinguished from topoisomerase binding to individual short DNA segments in the AFM images. Furthermore, the sequence of the DNA bound by the topoisomerase in these tripartite complexes was well defined, as were the lengths of the DNA segments on either side of the binding site, thus facilitating further analysis (See Supplementary Data). Substrates D3 and D4 resulted in a higher fraction of Topo IV bound to DNA in the AFM images. Whereas, it is conceivable that these substrates could affect the protein induced bending, footprinting experiments suggest that the protein protects ∼34 bp (34), and crystal structures of type IIA topoisomerases bound to DNA show that bending occurs ∼5 bp away from the cleavage sites (23,25). Furthermore, statistical analysis confirmed that the bend angles imposed on intact and

doubly nicked DNA segments by Topo IV were indistinguishable (see below).

For all four DNA substrates, we observed DNA bending when Topo IV was bound (Figures 5A, E and F). The included angle (ϕ) between the DNA segments emerging from the protein was measured as previously described (35,37–39), and the bend angle (θ) was defined as the supplement of ϕ, i.e. $\theta = 180° - \phi$ (Figures 1D and 5E). We determined bend angles for Topo IV bound to the four DNA substrates described above under several buffer conditions. Measured bend angles were normally distributed, and ANOVA and Tukey tests (44) of the bend angle distributions for intact and cleaved DNA substrates under all buffer conditions indicate that the populations were statistically indistinguishable (P_{ANOVA} and $P_{\text{Tukey}} > 0.05$). Hence, all data for Topo IV were combined and analyzed using maximum likelihood estimation (45) to determine the mean and standard deviation of the bend angle. We found that Topo IV bent the DNA by a mean angle of $80 \pm 3°$ with a SD = $30 \pm 2°$ ($n = 242$) (Figure 6A). The uncertainties represent the standard errors of the mean obtained from bootstrap analysis (46).

In addition to the manual tangent overlay method, we also used an automated tangent overlay method and an EED analysis to determine bend angles from the AFM images. Using the method of automated tangent overlay, we found that Topo IV bent the DNA by a mean angle of = $100 \pm 4°$ with a SD = $35 \pm 2°$ ($n = 181$) (Figure 6B). Using EED analysis we found that Topo IV bent DNA by a mean angle of $99 \pm 38°$ ($n = 242$) or $124 \pm 38°$
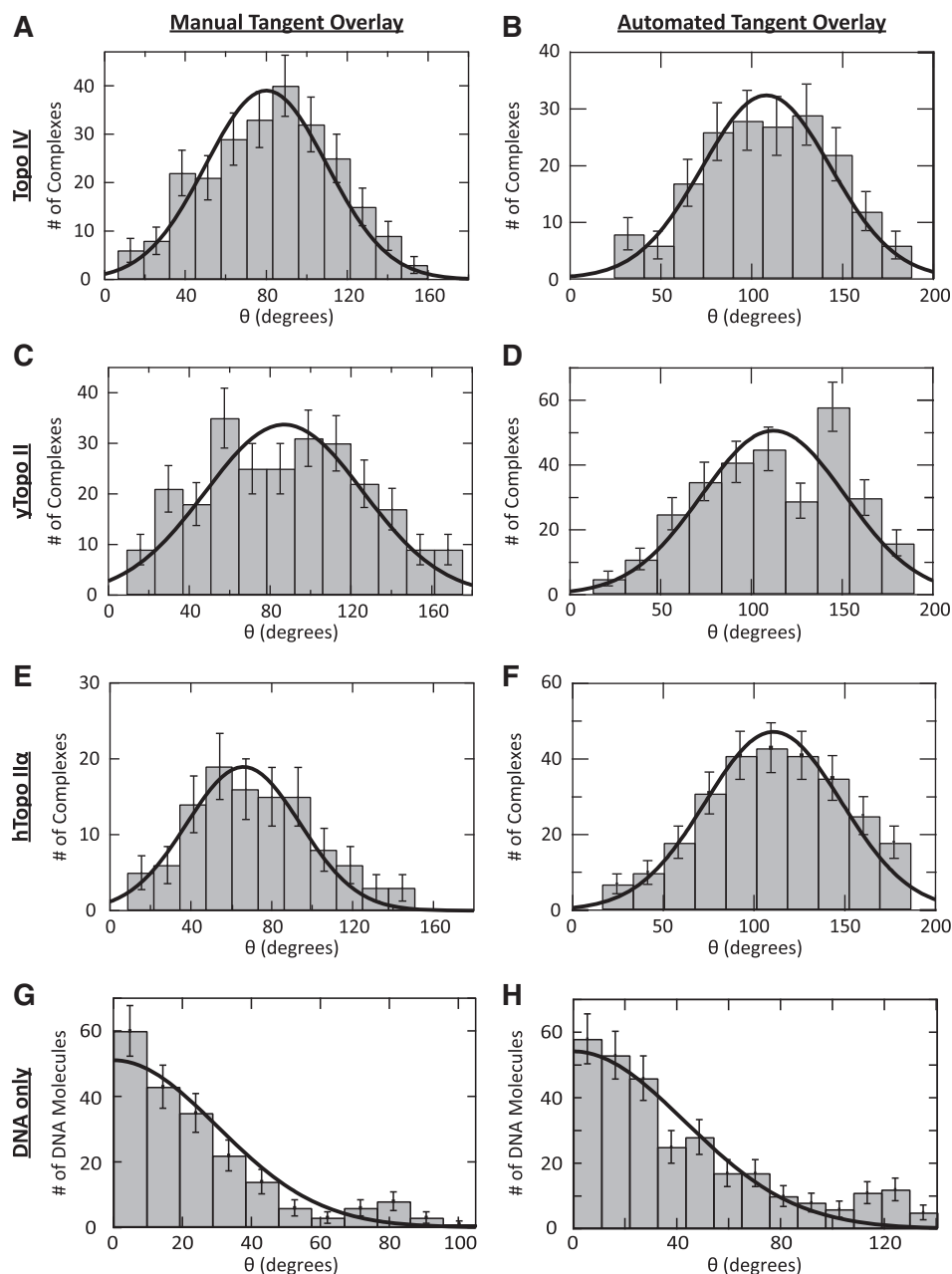
Figure 6. Distributions of bend angles imposed on DNA by different type IIA topoisomerases. Distribution of bend angles for Topo IV (**A**) determined by manual tangent overlay ($\mu = 80 \pm 3°$, $\sigma = 30 \pm 2°$, $n = 242$), and (**B**) determined by automated tangent overlay ($\mu = 100 \pm 4°$, $\sigma = 35 \pm 2°$, $n = 181$). Distribution of bend angles for yTopo II (**C**) determined by manual tangent overlay ($\mu = 87 \pm 5°$, $\sigma = 39 \pm 3°$, $n = 251$), and (**D**) determined by automated tangent overlay ($\mu = 103 \pm 4°$, $\sigma = 40 \pm 2°$, $n = 295$). Distribution of bend angles for hTopo IIα (**E**) determined by manual tangent overlay ($\mu = 66 \pm 4°$, $\sigma = 28 \pm 3°$, $n = 110$), and (**F**) determined by automated tangent overlay ($\mu = 102 \pm 5°$, $\sigma = 37 \pm 3°$, $n = 269$). Curves represent Gaussian distributions with parameters obtained from maximum likelihood fitting of the data with errors determined by bootstrapping (45,46). Distribution of bend angles for DNA in the absence of protein (**G**) determined by manual tangent overlay ($\mu = 0 \pm 1°$, $\sigma = 30 \pm 4°$, $n = 201$), and (**H**) determined by automated tangent overlay ($\mu = 0 \pm 1°$, $\sigma = 43 \pm 13°$, $n = 247$). These curves represent the best fit of a folded Gaussian distribution [Equation (3)] to the bend angle histograms with means and errors determined by bootstrapping (46–49).

($n = 181$), for manually and automatically selected populations of protein–DNA complexes, respectively.

Since the bend angles measured for Topo IV were independent of the DNA substrate, we used substrates D4 and D5, which is a symmetric version of D4 (Figure 2), to measure bending by yTopo II and hTopo IIα. Manual tangent overlay showed that yTopo II imposed a bend angle of $87 \pm 5°$ with a SD $= 39 \pm 3°$ ($n = 251$),

automated tangent overlay showed that yTopo II imposed a bend angle of $103 \pm 4°$ with a SD $= 40 \pm 2°$ ($n = 295$), and EED analysis showed that yTopo II imposed a bend angle of $105 \pm 35°$ ($n = 251$) or $103 \pm 35°$ ($n = 295$), depending on the population of protein-DNA complexes used (manually or automatically selected, respectively) (Figures 6C and D). Manual tangent overlay showed that hTopo IIα imposed a bend

Table 1. Bend angles measured from AFM images using four different analysis techniques and bend angles measured from single-molecule FRET

	Topo IV (°)	yTopo II (°)	hTopo IIα (°)
AFM			
Manual tangent[a]	80 ± 3	87 ± 5	66 ± 4
Automated tangent[a]	100 ± 4	103 ± 4	102 ± 5
EED histogram fit (manual)[b]	99 ± 38	105 ± 35	84 ± 32
Mean EED χ^2 (manual)[b]	102 ± 4	108 ± 7	81 ± 7
EED histogram fit (automated)[b]	123 ± 34	103 ± 17	126 ± 25
Mean EED χ^2 (automated)[b]	119 ± 6	102 ± 4	123 ± 4
Weighted mean of AFM measurements	94 ± 13	100 ± 7	95 ± 24
Single-molecule FRET	126 ± 18	140 ± 16	136 ± 17

[a]Mean ± SEM.
[b]θ ± angle at minimum $\chi^2 + 1$, $R_c = 6$ nm, see text.

angle of $66 \pm 4°$ with a SD = $28 \pm 3°$ ($n = 110$) (Figures 6E and F), automated tangent overlay showed that hTopo IIα imposed a bend angle of $102 \pm 5°$ with a SD = $37 \pm 3°$ ($n = 269$), and EED analysis showed that hTopo IIα imposed a bend angle of $84 \pm 32°$ ($n = 110$) or $127 \pm 32°$ ($n = 269$), depending on the population of protein–DNA complexes used (manually or automatically selected, respectively). The measured bend angles for each topoisomerase using each method are summarized in Table 1.

To determine the intrinsic bending of DNA on the mica surface, we imaged a 360 bp fragment of linear DNA (substrate D6, Figure 2) in the absence of protein (Figure 5D). We measured the bending of the DNA from the AFM images as previously described (35,38). Using ImageJ, circles were drawn near the middle of each DNA molecule to simulate bound protein. The bend angles were then measured using the angle measurement tool in ImageJ, as described above. Measurements of ϕ were assigned values <180°, resulting in a folded Gaussian distribution (47) of bend angles as described by Le Cam *et al.* (48) and Cherny *et al.* (49). The data were well fit by a folded Gaussian [Equation (3)], returning a mean (μ) of $0 \pm 1°$ and SD (σ) of $30 \pm 4°$ ($n = 201$) for bend angles measured using manual tangent overlay and a mean bend angle of $0 \pm 1°$ and SD = $43 \pm 13°$ ($n = 247$) for bend angles measured by the automated tangent overlay method (Figures 6G and H).

$$f(\mu, \sigma, \theta) = \frac{1}{\sigma\sqrt{2\pi}}\left(e^{-\frac{(\theta-\mu)^2}{2\sigma^2}} + e^{-\frac{(\theta+\mu)^2}{2\sigma^2}}\right) \tag{3}$$

In addition to the AFM measurements, we made single-molecule FRET measurements to estimate the bend angle imposed on DNA by each topoisomerase. Figure 7 shows the histograms of FRET efficiency values for each topoisomerase and a graph showing the relationship between FRET efficiency and DNA bend angle. The substrate we used for these experiments was the same substrate as used in the crystallization experiments done with yTopo II (25) with a single base change in the 4 bp overhang to disrupt its palindromic symmetry
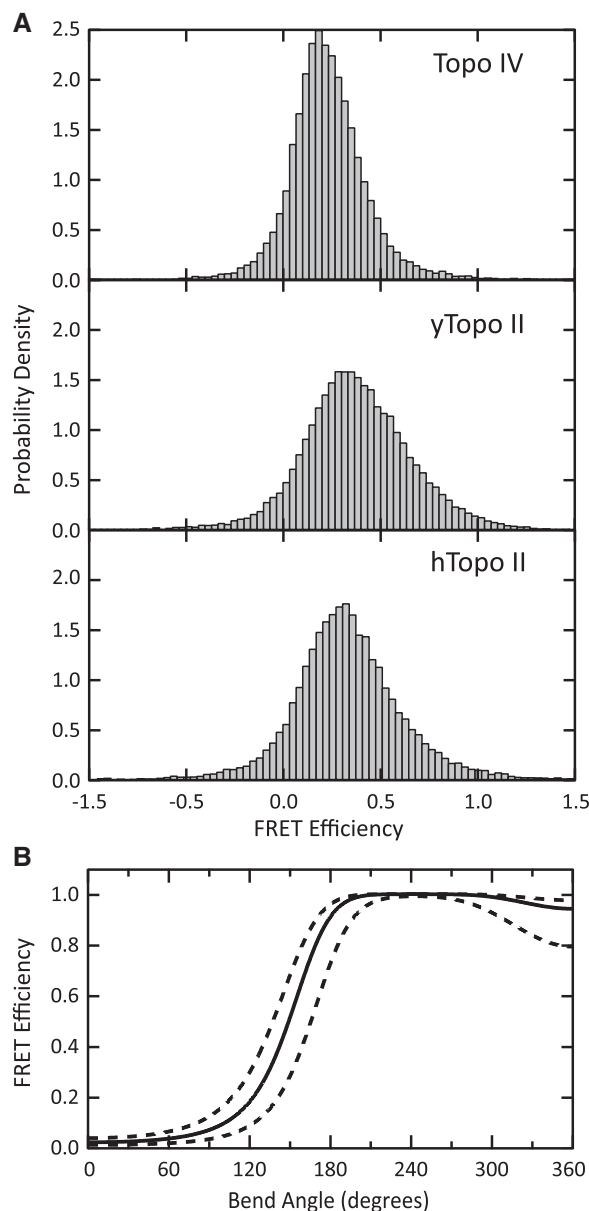

Figure 7. FRET efficiencies and relationship to DNA bend angle. (**A**) Histograms of FRET data for Topo IV (0.225 ± 0.007, $n = 20\,941$), yTopo II (0.370 ± 0.009, $n = 28\,363$) and hTopo IIα (0.324 ± 0.010, $n = 26\,593$) (mean ± SEM). (**B**) Plots showing FRET efficiency as a function of bend angle [Equations (4) and (5)] for the DNA substrate used in the FRET experiments using $R_0 = 7.4$, $r_c = 4.8$ nm, $r_{tot} = 14$ nm and $r_{rise} = 1.5$ nm (solid line) and the FRET efficiency versus bend angle relationship when experimental uncertainties, such as uncertainties in R_0 ($\pm 10\%$) and r_{rise} (± 1.5nm), are taken into account (dashed lines).

and a 30 bp extension, well separated from the binding site, to prevent the protein from interacting with the surface of the slide. The mean FRET efficiencies for Topo IV, yTopo II and hTopo IIα were $0.225 \pm .007$ ($n = 20\,941$), $0.370 \pm .009$ ($n = 28\,363$), and $0.324 \pm .010$ ($n = 26\,593$) (mean ± SEM), respectively (Figure 7A). We calculated the average fluorophore separation (r) from the measured FRET efficiencies using Equation (4) with a calculated R_0 value of 7.4 nm ± 10% for

the Alexa546-Alexa647 fluorophore pair used in the single-molecule FRET experiments. To calculate the imposed bend angle, we assumed the DNA geometry was similar to that observed in crystal structures (23–25,42). Accordingly, we modeled the bend as two symmetric bends (with bend angle $\theta/2$) on either side of a short DNA segment of length r_c between the two dyes separated by a total distance along the DNA of r_{tot} (Figure 3). In the analysis of our single-molecule FRET data, we included the possibility of a small helical pitch of the DNA. The inclusion of a significant helical pitch was a feature of the bend angle model. Klenin *et al.* (20) determined that the bend angle model was insensitive to the helical pitch when it exceeded a 9 nm helical rise over 150 bp, which corresponds to a rise per base pair of only 0.06 nm/bp. Because the protein contacts <40 bp of DNA, we estimated that the helical rise would be only on the order of ~3 nm over the biologically relevant length of DNA. We incorporated this DNA rise into the FRET calculations by introducing an additional term, r_{rise} into the equation for calculating r. We used a value of $r_{rise} = 1.5 \pm 1.5$ nm as the three possible cases representing zero helical rise, an intermediate 1.5 nm rise, and the ~3 nm helical rise assumed by the bend angle model (20). Equation (5) describes the relationship between the dye separation, r, and the geometry of the bent DNA. We calculated the separation between dyes on the DNA substrate, $r_{tot} = 14$ nm, assuming a length per base of 0.334 nm and based on the yTopo II crystal structure we set $r_c = 4.8$ nm (25). The resulting relationship between FRET efficiency and the bend angle θ is plotted in Figure 7B. With this model, the computed bend angles were $126 \pm 18°$ for Topo IV, $140 \pm 16°$ for yTopo II and $136 \pm 17°$ for hTopo IIα.

$$E_{\text{FRET}} = \frac{1}{1+\left(\frac{r}{R_0}\right)^6} \tag{4}$$

$$r = \sqrt{\left|r_c + (r_{tot} - r_c)\cos\left(\frac{\theta}{2}\right)\right|^2 + r_{rise}^2} \tag{5}$$

Although these bends are larger than those determined from the AFM images, the differences in the bend angles among the topoisomerases are very similar. These larger bend angles are more consistent with DNA bends determined from crystal structures (23–25,42). Importantly, the single-molecule FRET bend angle measurements were made in the same buffer in which the relaxation experiments were performed. We have observed that the composition of the buffer, particularly the ionic strength, changes not only the affinity but also the bend angle imposed by the topoisomerases. It is possible that the AFM deposition buffer, which was optimized to achieve equilibrated binding of the protein–DNA complexes onto the mica surface, contributed to the somewhat lower bend angles measured from the AFM images. Nevertheless, the FRET data and AFM data agree that the three Type IIA topoisomerases investigated here bend DNA to a similar degree.
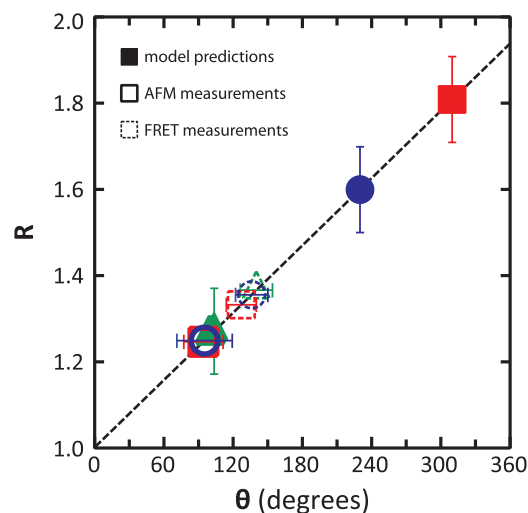

Figure 8. Comparison of measured and predicted bend angles imposed by type IIA topoisomerases. Shown is a plot of topology simplification ability (*R*) as a function of measured and predicted bend angles for Topo IV (red squares), yTopo II (green triangles) and hTopo IIα (blue circles). Bend angles measured from AFM images (outlined shapes) and FRET efficiencies (dashed outlined shapes) are plotted along with predicted bend angles extrapolated from the bend angle model (20) (solid shapes) using the non-equilibrium unknotting and supercoil relaxation data from Rybenkov *et al.* (15). (See Supplementary Data for a detailed description of the derivation of this relationship).

DISCUSSION

We have shown that the DNA bend angles imposed by Topo IV, hTopo IIα and yTopo II are similar and are not correlated with the extent of their topology simplification activities. This result is inconsistent with the bend angle model, in which the degree of topology simplification scales with the magnitude of the imposed bend angle (20). The relationship between topology simplification and bend angle determined by Klenin *et al.* (20) suggests that Topo IV should impose the largest bend angle (~310°), hTopo IIα should impose a smaller angle (~230°) and yTopo II should impose the smallest angle (~100°). (A detailed description of the derivation of the relationship between predicted bend angle and topology simplification is described in the Supplementary Data.) However, our AFM and single-molecule FRET data indicate that the three topoisomerases impose similar bend angles. Our AFM data suggested that yTopo II imposed the largest bend angle ($100 \pm 7°$), followed by hTopo IIα ($95 \pm 24°$), and lastly Topo IV ($94 \pm 13°$). Our FRET data suggest larger angles of $140 \pm 16°$ for yTopo II, $136 \pm 17°$ for hTopo IIα and $126 \pm 18°$ for Topo IV (Table 1, Figure 8). Within each technique, all three bend angles are within 15° of one another, which we consider to be within our experimental uncertainty. Also, the angles follow the opposite order of the predicted bend angles, and there is no evidence of the ~3–fold difference in bend angles required by the bend angle model (20). This leads us to conclude that while DNA bending is prevalent in all topoisomerases and may be an indicator of some conserved topology shifting mechanism, bending alone, within the context of the bend angle model, cannot

solely explain topology simplification by type IIA topoisomerases.

Though AFM measurements have consistently been shown to accurately measure protein–DNA interactions and conformations (35,37,50–53), we verified that deposition conditions favored 2D equilibration of the DNA molecules on the mica surface and hence that the data accurately represent the conformations of both the DNA and the protein-DNA complexes (54–56). 2D DNA equilibration is further supported by the agreement of bend angles determined by tangent measurements (both manual and automated) and EED measurements. Furthermore, the lack of correlation between the height of the DNA segments emerging from the protein and the measured bend angle is additional evidence that the protein–DNA complex equilibrated in 2D (see Supplementary Data).

Although direct visualization of DNA–type IIA topoisomerase complexes and measurement of bend angles have not been previously reported, other methods, such as protein–DNA co-crystalization, single-molecule DNA manipulation and DNA cyclization have been employed to probe topoisomerase-induced DNA bending. Crystal structures of several type IIA topoisomerase–DNA complexes have been reported in the literature. These include the TOPRIM fold, which is a conserved domain required for DNA cleavage, and primary DNA-binding domain of yTopo II (25,26), the breakage-reunion and TOPRIM domains of *S. pneumoniae* Topo IV in the presence of the quinolones moxifloxacin and clinafloxacin (23), and the ParE28-ParC58 fusion of *A. baumannii* Topo IV in the presence of the quinolone moxifloxacin (24). The yTopo II–DNA structure reported a DNA bend angle of ∼150°, and we estimated similar bend angles from the *S. pneumoniae* Topo IV–DNA crystal structure and the *A. baumannii* Topo IV–DNA crystal structure. In fact, the bend angle imposed on DNA by *A. baumannii* Topo IV, which has a high degree of sequence identity (61%) with *E. coli* Topo IV, was slightly smaller than the bend angle imposed on DNA by yTopo II, which is consistent with our results.

Our measurement of the bend angle imposed by yTopo II from AFM images (100 ± 7°) is smaller than the angle measured from the crystallized protein–DNA complex, though the angle measured from FRET experiments (140 ± 16°) is much closer to this value (∼150°) (25). The discrepancy could arise from several effects, including different buffer conditions used in AFM and single-molecule FRET experiments that could have affected the bend angles. FRET experiments were performed under the exact buffer conditions as the relaxation assays, whereas AFM experiments had to be performed in a buffer optimized for AFM deposition. We observed that monovalent salt concentration, in particular, had a strong influence on bend angle in our single-molecule FRET experiments (data not shown). Regardless of the discrepancies, our AFM and FRET data both show that type IIA topoisomerases bend DNA to a similar extent. This result is consistent with published DNA–topoisomerase crystal structures, which show that all crystallized protein–DNA complexes reveal comparable DNA

bending by type IIA topoisomerases from very different organisms (23–26,42). Though the exact role of DNA bending in the mechanism of type IIA topoisomerases has not been determined, one study suggests that these enzymes require the DNA to be under considerable strain in order for cleavage to occur (57). Perhaps DNA bending provides the necessary distortion of the double helix that allows the cleavage reaction and thereby the relaxation reaction to proceed.

The extent of DNA bending by Topo IV has also been estimated from single-molecule measurements of the size of plectonemic loops in supercoiled DNA with Topo IV bound, which indicate that Topo IV imposes a radius of curvature of ∼6.4 nm onto DNA (27). The radius of curvature can be related to a bend angle given assumptions about the distance over which the circular curvature approximation holds. A reasonable assumption is that the radius of curvature holds for an arc length equal to the number of DNA base pairs that interact with the protein. Estimating this length from footprinting data showing ∼34 bp of protected DNA (34), we calculated the bend angle could be as large as ∼135° (assuming the protein bends the DNA over 45 bp) or as small as ∼75° (assuming the protein bends the DNA over 25 bp). Our measured angle for Topo IV is consistent with this range. It should also be noted that the radius of curvature determined from the magnetic tweezers experiment is not consistent with a bend angle >180° and certainly not as large as the ∼310° angle suggested by the bend angle model. DNA bending by type IIA topoisomerases has also been probed through DNA cyclization experiments (19,21). Though these experiments have shown that Topo IV bends DNA and yTopo II does not, we noted in our AFM images, and others have observed (22), that type IIA topoisomerases have a high affinity for DNA ends. This renders the cyclization data difficult to interpret since the presence of a topoisomerase on the ends would likely confound the ligation reaction necessary to achieve cyclization.

Though the bend angle model was developed to explain non-equilibrium topology simplification, the sharp DNA bending predicted by the model has other implications. Klenin *et al.* (20) used Monte Carlo simulations to calculate the effects of sharply bent G–segment DNA on topoisomerase binding and activity. Many of these predictions have been addressed in subsequent publications, but their significance with respect to the bend angle model has not been discussed. For instance, the bend angle model suggests that a sharp bend imposed on DNA by Topo IV would result in a twenty fold higher binding affinity for positively supercoiled [(+)sc] DNA than for negatively supercoiled [(–)sc] DNA. However, the binding affinity of Topo IV for (+)sc and (–)sc DNA is the same or at most a factor of ∼3 larger for (+)sc DNA (58–60). A large bend angle imposed by Topo IV would also provide a mechanism to explain the higher efficiency of Topo IV in relaxing (+)sc DNA than (–)sc DNA (58–60). However, recent work suggests that chiral discrimination by Topo IV results from differences in processivity rather than initial binding differences (59). Moreover, hTopo IIα has also been shown to relax (+)sc DNA an

order of magnitude more efficiently than (–)sc DNA, yet its binding affinity is slightly higher for (–)sc DNA (61). The bend angle model also predicts that Topo IV should localize at apices of supercoils 87% of the time for (–) supercoils, but only 28% of the time for (+) supercoils (20). Whereas this prediction has not been directly tested, data from magnetic tweezers pulling assays suggest that Topo IV has a 50% or higher affinity for (+) supercoil plectoneme apices (27). Furthermore, recent simulation data using an improved WLC model for DNA has shown that a DNA hairpin, i.e. a sharp bend formed by a topoisomerase, is not sufficient to reproduce the experimentally observed degree of topology simplification (28,29). Measurements of the DNA circle size dependence of non-equilibrium relaxation provide additional evidence suggesting that the bend angle model does not completely describe non-equilibrium topological relaxation (6,16,21). The impact of DNA bending, and therefore the efficiency of the non-equilibrium relaxation process, would be expected to increase as the DNA circle size decreases. However, experiments with yTopo II and Topo IV show that the topology simplification activity decreases with circle size for small DNA circles and is independent of circle size for larger DNA circles. The ensemble of the available evidence from previous studies and from the measurements of the bend angle presented here suggests that the bend angle model cannot fully account for the observed non-equilibrium relaxation activity of type IIA topoisomerases. However, it is possible that non-equilibrium relaxation results from G–segment bending in combination with a second mechanism. All three topoisomerases were found to impose comparable bends onto DNA, which suggests that the bend angle model is incapable of explaining the measured differences between the topology simplification abilities of these three enzymes. However, these bend angles are somewhat consistent with the degree of bending expected from the least capable topology simplifier, yTopo II. Thus, it is conceivable that DNA bending is a conserved mechanism that is able to account for the base level of topology simplification achievable by type IIA topoisomerases. Further levels of topology simplification, as found in Topo IV and hTopo IIα, must arise from an additional enzyme specific mechanism, likely unrelated to DNA bending.

Several other models have been proposed to explain the topology simplification mechanism of type IIA topoisomerases (22). A tracking model proposes that the enzyme binds to a DNA crossing and tracks along the DNA to trap T–segments that are catenated or knotted (15). However, an experiment that placed tightly bound protein 'roadblocks' at several locations along supercoiled circular DNA did not affect non-equilibrium supercoil relaxation (16). A three segment binding model postulates that the topoisomerase binds two potential T–segments prior to selecting one for strand-passage based on local geometry (21). However, this model predicts an asymmetric removal of positive versus negative supercoils that would result in a skewed topoisomer distribution, which we did not observe for any of the type IIA topoisomerases studied (Figure 4). Other studies have also failed

to detect asymmetric supercoil removal by type IIA topoisomerases (16), so while this model may hold in certain cases, it does not explain the more general mechanism of topology simplification. Two compelling possibilities are the hooked juxtaposition model and the kinetic proofreading model. The hooked juxtaposition model postulates that type IIA topoisomerases detect and relax specific juxtapositions of catenated, knotted and supercoiled DNA in which the G– and T–segments are bent toward one another (17). Simulations based on lattice and WLC models indicate that strand passage at these hooked juxtapositions is sufficient to produce non-equilibrium topology simplification (28,29,62–64). The kinetic proofreading model suggests that upon binding to the G–segment of DNA and encountering an initial T–segment, the topoisomerase becomes transiently activated, perhaps by binding one of the two ATP molecules. The T–segment is released and strand passage will occur if a second T–segment is captured while the enzyme remains in the active state (18,65). It is possible that one of these models, perhaps coupled with the small effect arising from the bend angles imposed by the topoisomerase, could account for the non-equilibrium topology simplification activity of type IIA topoisomerases. The relatively sharp bend imposed on the G–segment DNA by type IIA topoisomerases is consistent with the hooked juxtaposition model, though it remains to be determined if bent T–segments are preferentially captured and passed. Further experiments are necessary to test these models to determine which, if either, can explain this fascinating phenomenon.

REFERENCES

1. Berger,J.M. (1998) Type II DNA topoisomerases. *Curr. Opin. Struct. Biol.*, **8**, 26–32.
2. Champoux,J.J. (2001) DNA topoisomerases: structure, function and mechanism. *Annu. Rev. Biochem.*, **70**, 369–413.
3. Wang,J.C. (2002) Cellular roles of DNA topoisomerases: a molecular perspective. *Nat. Rev. Mol. Cell. Biol.*, **3**, 430–440.
4. Forterre,P., Gribaldo,S., Gadelle,D. and Serre,M.C. (2007) Origin and evolution of DNA topoisomerases. *Biochimie*, **89**, 427–446.
5. Deweese,J.E. and Osheroff,N. (2009) The DNA cleavage reaction of topoisomerase II: wolf in sheep's clothing. *Nucleic Acids Res.*, **37**, 738–748.
6. Bates,A.D. and Maxwell,A. (2007) Energy coupling in Type II topoisomerases: why do they hydrolyze ATP? *Biochemistry*, **46**, 7929–7941.
7. Schoeffler,A.J. and Berger,J.M. (2008) DNA topoisomerases: harnessing and constraining energy to govern chromosome topology. *Q. Rev. Biophys.*, **41**, 41–101.
8. Buhler,C., Lebbink,J.H., Bocs,C., Ladenstein,R. and Forterre,P. (2001) DNA topoisomerase VI generates ATP-dependent double-strand breaks with two-nucleotide overhangs. *J. Biol. Chem.*, **276**, 37215–37222.
9. Corbett,K.D. and Berger,J.M. (2003) Structure of the topoisomerase VI-B subunit: implications for Type II topoisomerase mechanism and evolution. *EMBO J.*, **22**, 151–163.
10. Corbett,K.D., Benedetti,P. and Berger,J.M. (2007) Holoenzyme assembly and ATP-mediated conformational dynamics of topoisomerase VI. *Nat. Struct. Mol. Biol.*, **14**, 611–619.
11. Liu,Z.R., Deibler,R.W., Chan,H.S. and Zechiedrich,L. (2009) The why and how of DNA unlinking. *Nucleic Acids Res.*, **37**, 661–671.
12. Ishii,S., Murakami,T. and Shishido,K. (1991) Gyrase inhibitors increase the content of knotted DNA species of plasmid pBR322 in *E. coli. J. Bacteriol.*, **173**, 5551–5553.
13. Shishido,K., Komiyama,N. and Ikawa,S. (1987) Increased production of a knotted form of plasmid pBR322 DNA in *Escherichia coli* DNA topoisomerase mutants. *J. Mol. Biol.*, **195**, 215–218.
14. Deibler,R.W., Mann,J.K., Sumners,D.W.L. and Zechiedrich,L. (2007) Hin-mediated DNA knotting and recombining promote replicon dysfunction and mutation. *BMC Mol. Biol.*, **8**, 44.
15. Rybenkov,V.V., Ullsperger,C., Vologodskii,A.V. and Cozzarelli,N.R. (1997) Simplification of DNA topology below equilibrium values by Type II topoisomerases. *Science*, **277**, 690–693.
16. Stuchinskaya,T., Mitchenall,L.A., Schoeffler,A.J., Corbett,K.D., Berger,J.M., Bates,A.D. and Maxwell,A. (2009) How do Type II topoisomerases use ATP hydrolysis to simplify DNA topology beyond equilibrium? Investigating the relaxation reaction of nonsupercoiling Type II topoisomerases. *J. Mol. Biol.*, **385**, 1397–1408.
17. Buck,G.R. and Zechiedrich,E.L. (2004) DNA disentangling by Type-2 topoisomerases. *J. Mol. Biol.*, **340**, 933–939.
18. Yan,J., Magnasco,M.O. and Marko,J.F. (1999) A kinetic proofreading mechanism for disentanglement of DNA by topoisomerases. *Nature*, **401**, 932–935.
19. Vologodskii,A.V., Zhang,W., Rybenkov,V.V., Podtelezhnikov,A.A., Subramanian,D., Griffith,J.D. and Cozzarelli,N.R. (2001) Mechanism of topology simplification by Type II DNA topoisomerases. *Proc. Natl Acad. Sci. USA*, **98**, 3045–3049.
20. Klenin,K., Langowski,J. and Vologodskii,A. (2002) Computational analysis of the chiral action of Type II DNA topoisomerases. *J. Mol. Biol.*, **320**, 359–367.
21. Trigueros,S., Salceda,J., Bermudez,I., Fernandez,X. and Roca,J. (2004) Asymmetric removal of supercoils suggests how topoisomerase II simplifies DNA topology. *J. Mol. Biol.*, **335**, 723–731.
22. Vologodskii,A. (2009) Theoretical models of DNA topology simplification by Type IIA DNA topoisomerases. *Nucleic Acids Res.*, **37**, 3125–3133.
23. Laponogov,I., Sohi,M.K., Veselkov,D.A., Pan,X.S., Sawhney,R., Thompson,A.W., McAuley,K.E., Fisher,L.M. and Sanderson,M.R. (2009) Structural insight into the quinolone-DNA cleavage complex of Type IIA topoisomerases. *Nat. Struct. Mol. Biol.*, **16**, 667–669.
24. Wohlkonig,A., Chan,P.F., Fosberry,A.P., Homes,P., Huang,J., Kranz,M., Leydon,V.R., Miles,T.J., Pearson,N.D., Perera,R.L. *et al.* (2010) Structural basis of quinolone inhibition of Type IIA topoisomerases and target-mediated resistance. *Nat. Struct. Mol. Biol.*, **17**, 1152–1153.
25. Dong,K.C. and Berger,J.M. (2007) Structural basis for gate-DNA recognition and bending by Type IIA topoisomerases. *Nature*, **450**, 1201–1205.
26. Schmidt,B.H., Burgin,A.B., Deweese,J.E., Osheroff,N. and Berger,J.M. (2010) A novel and unified two-metal mechanism for DNA cleavage by Type II and IA topoisomerases. *Nature*, **465**, 641–644.
27. Charvin,G., Strick,T.R., Bensimon,D. and Croquette,V. (2005) Topoisomerase IV bends and overtwists DNA upon binding. *Biophys. J.*, **89**, 384–392.
28. Liu,Z.R., Zechiedrich,L. and Chan,H.S. (2010) Local site preference rationalizes disentangling by DNA topoisomerases. *Phys. Rev. E*, **81**, 031902.
29. Liu,Z.R., Zechiedrich,L. and Chan,H.S. (2010) Action at hooked or twisted-hooked DNA juxtapositions rationalizes unlinking preference of Type-2 topoisomerases. *J. Mol. Biol.*, **400**, 963–982.
30. Elsea,S.H., Hsiung,Y., Nitiss,J.L. and Osheroff,N. (1995) A yeast Type II topoisomerase selected for resistance to quinolones. Mutation of histidine 1012 to tyrosine confers resistance to nonintercalative drugs but hypersensitivity to ellipticine. *J. Biol. Chem.*, **270**, 1913–1920.
31. Kingma,P.S., Greider,C.A. and Osheroff,N. (1997) Spontaneous DNA lesions poison human topoisomerase II alpha and stimulate cleavage proximal to leukemic 11q23 chromosomal breakpoints. *Biochemistry*, **36**, 5934–5939.
32. Corbett,K.D., Schoeffler,A.J., Thomsen,N.D. and Berger,J.M. (2005) The structural basis for substrate specificity in DNA topoisomerase IV. *J. Mol. Biol.*, **351**, 545–561.
33. Tropea,J.E., Cherry,S. and Waugh,D.S. (2009) Expression and purification of soluble His(6)-tagged TEV protease. *Methods Mol. Biol.*, **498**, 297–307.
34. Marians,K.J. and Hiasa,H. (1997) Mechanism of quinolone action. A drug-induced structural perturbation of the DNA precedes strand cleavage by topoisomerase IV. *J. Biol. Chem.*, **272**, 9401–9409.
35. Wang,H., Yang,Y., Schofield,M.J., Du,C.W., Fridman,Y., Lee,S.D., Larson,E.D., Drummond,J.T., Alani,E., Hsieh,P. *et al.* (2003) DNA bending and unbending by MutS govern mismatch recognition and specificity. *Proc. Natl Acad. Sci. USA*, **100**, 14822–14827.
36. Horcas,I., Fernandez,R., Gomez-Rodriguez,J.M., Colchero,J., Gomez-Herrero,J. and Baro,A.M. (2007) WSXM: a software for scanning probe microscopy and a tool for nanotechnology. *Rev. Sci. Instrum.*, **78**, 013705.
37. Erie,D.A., Yang,G., Schultz,H.C. and Bustamante,C. (1994) DNA bending by Cro protein in specific and nonspecific complexes: implications for protein site recognition and specificity. *Science*, **266**, 1562–1566.
38. Rees,W.A., Keller,R.W., Vesenka,J.P., Yang,G. and Bustamante,C. (1993) Evidence of DNA bending in transcription complexes imaged by scanning force microscopy. *Science*, **260**, 1646–1649.
39. Allan,B.W., Garcia,R., Maegley,K., Mort,J., Wong,D., Lindstrom,W., Beechem,J.M. and Reich,N.O. (1999) DNA bending by EcoRI DNA methyltransferase accelerates base flipping but compromises specificity. *J. Biol. Chem.*, **274**, 19269–19275.
40. Dame,R.T., van Mameren,J., Luijsturburg,M.S., Mysiak,M.E., Janicijevic,A., Pazdzior,G., van der Vliet,P.C., Wyman,C. and Wuite,G.J. (2005) Analysis of scanning force microscopy images of protein-induced DNA bending using simulations. *Nucleic Acids Res.*, **33**, e68.
41. Almeida,F.M.L., Barbi,M. and do Vale,M.A.B. (2000) A proposal for a different chi-square function for Poisson distributions. *Nucl. Instrum. Methods Phys. Res. Sect. A-Accel. Spectrom. Dect. Assoc. Equip.*, **449**, 383–395.

42. Laponogov,I., Pan,X.S., Veselkov,D.A., McAuley,K.E., Fisher,L.M. and Sanderson,M.R. (2010) Structural basis of gate-DNA breakage and resealing by Type II topoisomerases. *PLoS One*, **5**, e11338.
43. Rivetti,C., Walker,C. and Bustamante,C. (1998) Polymer chain statistics and conformational analysis of DNA molecules with bends or sections of different flexibility. *J. Mol. Biol.*, **280**, 41–59.
44. Sokal,R.R. and Rohlf,F.J. (1969) *Biometry*. W. H. Freeman and Company, San Francisco, CA.
45. Bevington,P. and Robinson,K.D. (2002) *Data Reduction and Error Analysis for the Physical Sciences*, 3rd edn. McGraw-Hill Science/Engineering/Math, New York, NY.
46. Efron,B. and Tibshirani,R. (1991) Statistical data analysis in the computer age. *Science*, **253**, 390–395.
47. Leone,F.C., Nottingham,R.B. and Nelson,L.S. (1961) Folded normal distribution. *Technometrics*, **3**, 543–550.
48. Le Cam,E., Fack,F., Menissier-de Murcia,J., Cognet,J.A., Barbin,A., Sarantoglou,V., Revet,B., Delain,E. and de Murcia,G. (1994) Conformational analysis of a 139 base-pair DNA fragment containing a single-stranded break and its interaction with human poly(ADP-ribose) polymerase. *J. Mol. Biol.*, **235**, 1062–1071.
49. Cherny,D.I., Striker,G., Subramaniam,V., Jett,S.D., Palecek,E. and Jovin,T.M. (1999) DNA bending due to specific p53 and p53 core domain-DNA interactions visualized by electron microscopy. *J. Mol. Biol.*, **294**, 1015–1026.
50. Lu,Y., Weers,B.D. and Stellwagen,N.C. (2003) Analysis of the intrinsic bend in the M13 origin of replication by atomic force microscopy. *Biophys. J.*, **85**, 409–415.
51. Pastre,D., Hamon,L., Sorel,I., Le Cam,E., Curmi,P.A. and Pietrement,O. (2009) Specific DNA-protein interactions on mica investigated by atomic force microscopy. *Langmuir*, **26**, 2618–2623.
52. Bustamante,C. and Rivetti,C. (1996) Visualizing protein-nucleic acid interactions on a large scale with the scanning force microscope. *Annu. Rev. Biophys. Biomol. Struct.*, **25**, 395–429.
53. Rivetti,C., Guthold,M. and Bustamante,C. (1999) Wrapping of DNA around the *E.coli* RNA polymerase open promoter complex. *EMBO J.*, **18**, 4464–4475.
54. Faas,F.G., Rieger,B., van Vliet,L.J. and Cherny,D.I. (2009) DNA deformations near charged surfaces: electron and atomic force microscopy views. *Biophys J.*, **97**, 1148–1157.
55. Bustamante,C., Marko,J.F., Siggia,E.D. and Smith,S. (1994) Entropic elasticity of lambda-phage DNA. *Science*, **265**, 1599–1600.
56. Rivetti,C., Guthold,M. and Bustamante,C. (1996) Scanning force microscopy of DNA deposited onto mica: equilibration versus kinetic trapping studied by statistical polymer chain analysis. *J. Mol. Biol.*, **264**, 919–932.
57. Deweese,J.E. and Osheroff,N. (2009) Coordinating the two protomer active sites of human topoisomerase IIalpha: nicks as topoisomerase II poisons. *Biochemistry*, **48**, 1439–1441.
58. Charvin,G., Strick,T.R., Bensimon,D. and Croquette,V. (2005) Tracking topoisomerase activity at the single-molecule level. *Annu. Rev. Biophys. Biomol. Struct.*, **34**, 201–219.
59. Neuman,K.C., Charvin,G., Bensimon,D. and Croquette,V. (2009) Mechanisms of chiral discrimination by topoisomerase IV. *Proc. Natl Acad. Sci. USA*, **106**, 6986–6991.
60. Stone,M.D., Bryant,Z., Crisona,N.J., Smith,S.B., Vologodskii,A., Bustamante,C. and Cozzarelli,N.R. (2003) Chirality sensing by *Escherichia coli* topoisomerase IV and the mechanism of type II topoisomerases. *Proc. Natl Acad. Sci. USA*, **100**, 8654–8659.
61. McClendon,A.K., Rodriguez,A.C. and Osheroff,N. (2005) Human topoisomerase IIalpha rapidly relaxes positively supercoiled DNA: implications for enzyme action ahead of replication forks. *J. Biol. Chem.*, **280**, 39337–39345.
62. Randall,G.L., Pettitt,B.M., Buck,G.R. and Zechiedrich,E.L. (2006) Electrostatics of DNA-DNA juxtapositions: consequences for type II topoisomerase function. *J. Phys.-Condens. Matter*, **18**, S173–S185.
63. Liu,Z.R., Mann,J.K., Zechiedrich,E.L. and Chan,H.S. (2006) Topological information embodied in local juxtaposition geometry provides a statistical mechanical basis for unknotting by type-2 DNA topoisomerases. *J. Mol. Biol.*, **361**, 268–285.
64. Liu,Z.R., Zechiedrich,E.L. and Chan,H.S. (2006) Inferring global topology from local juxtaposition geometry: interlinking polymer rings and ramifications for topoisomerase action. *Biophys. J.*, **90**, 2344–2355.
65. Yan,J., Magnasco,M.O. and Marko,J.F. (2001) Kinetic proofreading can explain the supression of supercoiling of circular DNA molecules by type-II topoisomerases. *Phys. Rev. E. Stat. Nonlin. Soft. Mat. Phys.*, **63**, 031909.